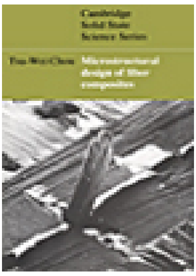

Microstructural Design of Fiber Composites

Tsu-Wei Chou

Book DOI: http://dx.doi.org/10.1017/CBO9780511600272

Online ISBN: 9780511600272

Hardback ISBN: 9780521354820

Paperback ISBN: 9780521019651

Chapter

8 - Flexible composites pp. 443-473

Chapter DOI: http://dx.doi.org/10.1017/CBO9780511600272.009

Cambridge University Press

8 Flexible composites

8.1 Introduction

The term 'flexible composites' is used hereinafter to identify composites based upon elastomeric polymers of which the usable range of deformation is much larger than those of the conventional thermosetting or thermoplastic polymer-based composites (Chou and Takahashi 1987). The ability of flexible composites to sustain large deformation and fatigue loading and still provide high load-carrying capacity has been mainly analyzed in pneumatic tire and conveyor belt constructions. However, the unique capability of flexible composites is yet to be explored and investigated. This chapter examines the fundamental characteristics of flexible composites.

Besides tires and conveyor belts, flexible composites can be found in a wide range of applications. Coated (with PVC, Teflon, rubber, etc.) fabrics have been used for air- or cable-supported building structures, tents, parachutes, decelerators in high speed airplanes, bullet-proof vests, tarpaulin inflated structures such as boats and escape slides, safety nets, and other inexpensive products. Hoses, flexible diaphragms, racket strings, surgical replacements, geotextiles, and reinforced membrane structures in general are examples of flexible composites.

Following Chou (1989, 1990), the nonlinear elastic behavior of three categories of materials is examined: pneumatic tires, coated fabrics, and flexible composites containing wavy fibers. These materials provide the model systems of analysis with elastic behaviors ranging from small to large deformations.

The performance characteristics of pneumatic tires are primarily controlled by the anisotropic properties of the cord/rubber composite. The low modulus, high elongation rubber contains the air and provides abrasion resistance and road grip. The high modulus, low elongation cords carry most of the loads applied to the tire in service. According to Walter (1978), the first quantitative study of cord/rubber elastic properties in the tire industry was published in Germany by Martin (1939), who analyzed bias ply aircraft tires using thin shell theory to approximate toroidal tire behavior.

Martin's analysis of the orthotropic composite elastic constants assumes that the fibers are inextensible and the matrix stiffness is negligibly small; this approach has been referred to here as the *classical netting analysis*. Studies of the cord/rubber properties became active worldwide in the 1960s as represented by the work of Clark (1963a&b, 1964) in the USA, Gough (1968) in Great Britain, Akasaka (1959–64) in Japan, and Biderman *et al.* (1963) in the Soviet Union.

The existing analysis on tire mechanics is primarily based upon the well developed anisotropic theory of rigid laminated composites for small linear elastic deformation. Thus, the problems of viscoelasticity, strength behavior, fatigue and large non-linear behavior are often ignored.

In the case of coated fabrics, limited attention has been given to the material stress–strain response to arbitrary loading paths and histories. Experimental studies of the biaxial stress–strain behavior can be found in the works of Skelton (1971), Alley and Fairslon (1972) and Reindhardt (1976). Attempts have also been made by Akasaka and Yoshida (1972) and by Stubbs and Thomas (1984) to analytically model the elastic and inelastic properties of coated fabrics under biaxial loading. Some of these results are briefly recapitulated in this chapter.

Section 8.4 focusses on the understanding of the large nonlinear deformation of flexible composites. To this end, model material systems for analytical purposes need to be identified. The large nonlinear deformation could originate from two sources, i.e. matrix and fiber. In order to fully realize the ability of the elastomeric matrix to sustain large deformation, the fibers must be able to deform accordingly with the matrix. This can be achieved by (a) using short fibers, (b) arranging continuous fibers in such an orientation that they are allowed to rotate as the load increases, and (c) using reinforcements in woven, knitted, braided, or other wavy forms.

Possibility (c) is particularly interesting in that it utilizes the waviness of the fibers. The gradual straightening of the wavy fibers under external loading results in enhanced stiffness with an increase in deformation. The linear and nonlinear elastic behavior of two- and three-dimensional textile structural composites has been examined by Ishikawa and Chou (1983), Chou (1985), and Chou and Yang (1986) based on small deformation theory. The nonlinear finite deformation analyses of flexible composites are presented in Chapter 9.

8.2 Cord/rubber composites

Cord/rubber composites for pneumatic tires are examined in this section from the viewpoint of the mechanics of anisotropic materials. Cord/rubber composites are complex elastomeric composites composed of (a) the rubber matrix of usually quite low modulus and high extensibility, (b) the reinforcing cord of much higher modulus and lower extensibility than the matrix, and (c) the adhesive film which bonds the cord to the matrix. The combination is subjected to (a) fluctuating loads, mostly tensile but on occasion compressive, (b) temperatures as high as 125°C, and (c) moisture. Obviously substantial stress develops at the cord-rubber interface. Some of the discussions presented herein on the materials and mechanics aspects of pneumatic tires are based upon the review articles of Walter (1978) and Clark (1980).

The construction of tires involves calendering sheets of rubber around an array of parallel textile cords to form a flat, essentially two-dimensional anisotropic sheet. The cords usually have substantial twist and often are made up of two or three oppositely twisted yarns. These composite sheets are then assembled into various tire configurations. Figure 8.1(a) shows the typical bias or angle-ply design which utilizes two or more, usually an even number, of plies laid at alternate diagonal angles to one another. Figure 8.1(b) depicts a typical radial tire construction involving radially oriented cords while the tread area is reinforced by a belt structure of relatively small angle with respect to the tire center line. The radial tire construction provides stiff longitudinal reinforcement for the tread area (and, hence, is less subject to slip) and flexibility for the vertical deflection. In the terminology of laminated composites, bias

Fig. 8.1. (a) Bias tire. (b) Radial ply tire. (After Clark 1980.)

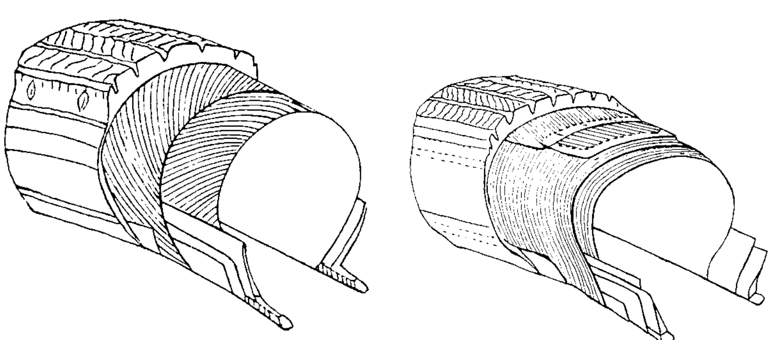

(a) (b)

and radial tires can be categorized as laminates with $[+\theta/-\theta]$ and $[+\theta/-\theta/90°]$ orientations with respect to the tire center line.

8.2.1 *Rubber and cord properties*

For relatively small strain, rubber may be treated as a homogeneous and isotropic material. The Young's modulus, determined from the initial slope of the stress–strain curve, may be as low as 0.69 MPa (100 psi) for non-reinforced (unfilled) elastomers to as high as 689 MPa (100 000 psi) for highly vulcanized (high sulfur) compounds such as ebonite. The Young's modulus of rubber is affected by the conditions of physical testing (i.e. strain rate, temperature, cyclic load history) and chemical vulcanization parameters (i.e. the compounding ingredients, state of cure) (see Clark 1980).

The assumption of negligible volume change of rubber leads to the following values of Poisson's ratio (ν), bulk modulus (K), Young's modulus (E) and shear modulus (G):

$$\begin{aligned} &\nu \approx \tfrac{1}{2} \\ &K \rightarrow \infty \\ &E \approx 3G \end{aligned} \tag{8.1}$$

Rubbers used in calendered plies of tires have E values of 5.51 MPa (800 psi) for textile body ply, 20.67 MPa (3000 psi) for textile tread ply and 13.78 MPa (2000 psi) for steel tread ply. The ν value for these materials is 0.49.

The Young's moduli for tire cords vary with cord constructions. The following values are for belt ply: 109.55 GPa (15.9×10^6 psi) for steel, 24.8 GPa (3.6×10^6 psi) for Kevlar, and 11.02 GPa (1.6×10^6 psi) for rayon. The values for body ply are: 3.96 GPa (575×10^3 psi) for polyester, and 3.45 GPa (500×10^3 psi) for nylon. Experiments have shown that textile cords can carry some load in compression, although compressive loads are believed to be the source of many textile failures and should be avoided whenever possible.

Twisting of the cord is needed in order to provide adequate cord fatigue life under service conditions. However, twisting of fiber into tire cord can result in as much as a one-third decrease in tensile Young's modulus for belt ply cords, and a one-half decrease in Young's modulus for body ply cord. It has been predicted that the axial Young's modulus of a single twisted fiber yarn is approximately equal to $1/(1 + 4\pi^2 R^2 T^2)$ of that of the untwisted yarn. Here, R and T denote yarn radius and twist (number of turns per unit length), respectively (Hearle, Grosberg and Backer 1969). The twisted and multi-plied cords should be considered as transversely isotropic, although they are commonly approximated as isotropic. Textile cords normally show substantial nonlinearity in their stress–strain behavior. However, since the rubber behavior is relatively elastic in the small strain range, and the cords in a laminate are often aligned at an angle to the load direction, the composite acts more like a linearly elastic solid than the cord itself. Figure 8.2 shows the stress–strain curve of a tubular specimen using rayon yarn in a rubber matrix. The fibers in this specimen are in angle-ply arrangement. According to Clark (1980), most pneumatic tires do not operate with strain much in excess of 10%.

8.2.2 *Unidirectional composites*

The linear elastic behavior of a unidirectional cord/rubber composite can be easily deduced from the basic equations given in Section 2.2. By assuming that

$$\begin{aligned} E_f &\gg E_m \\ \nu_m &= 0.5 \end{aligned} \tag{8.2}$$

Fig. 8.2. Load–strain curve of a cylindrical tube with rayon yarns in a rubber matrix. (After Clark 1980.)

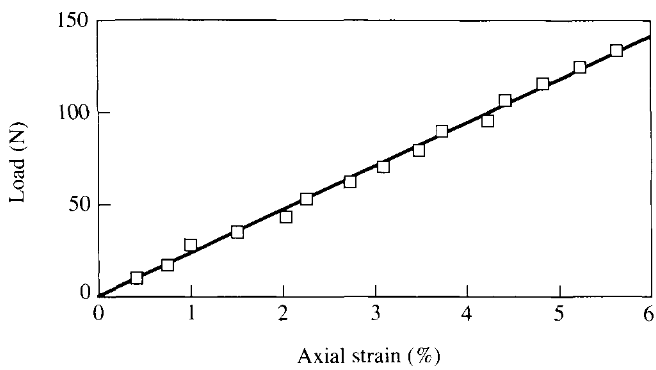

The following relations can be obtained:

$$
\begin{aligned}
&E_{11} = E_f V_f \gg E_{22} \\
&\nu_{21} = 0 \\
&E_{22} = c_1 \frac{E_m}{V_m} = \frac{(1+1.3V_f)}{(1+0.5V_f)} \frac{E_m}{V_m} \\
&G_{12} = c_2 \frac{G_m}{V_m} = (1+V_f) \frac{G_m}{V_m}
\end{aligned}
\tag{8.3}
$$

where c_1 and c_2 denote two coefficients.

Akasaka (1989) considered the same assumptions as Eqs. (8.2) and obtained the simpler form slightly different from Eqs. (8.3), with the coefficients $c_1 = \frac{4}{3}$ and $c_2 = 1$. Then,

$$
\begin{aligned}
&E_{22} \approx \frac{4}{3} \frac{E_m}{V_m} \\
&G_{12} \approx \frac{G_m}{V_m} \approx \frac{E_{22}}{4}
\end{aligned}
\tag{8.4}
$$

Akasaka (1989) has noted that the relation of $G_{12} \approx E_{22}/4$ is independent of cord volume fraction and has good predictability as compared to existing formulas and experimental results (Walter and Patel 1979; Clark 1980). Also, $c_1 = c_2 = 1$ has been used by Jones (1975).

Based upon Eqs. (8.4), the variation of lamina transformed reduced stiffness with cord off-axis angle θ follows from Eqs. (2.16) and can be approximated as (Akasaka and Hirano 1972):

$$
\begin{aligned}
&\bar{Q}_{11} \approx E_{22} + E_{11} \cos^4 \theta \\
&\bar{Q}_{22} \approx E_{22} + E_{11} \sin^4 \theta \\
&\bar{Q}_{66} \approx E_{22}/4 + E_{11} \sin^2 \theta \cos^2 \theta \\
&\bar{Q}_{12} \approx E_{22}/2 + E_{11} \sin^2 \theta \cos^2 \theta \\
&\bar{Q}_{16} \approx E_{11} \sin \theta \cos^3 \theta \\
&\bar{Q}_{26} \approx E_{11} \sin^3 \theta \cos \theta
\end{aligned}
\tag{8.5}
$$

When a unidirectional cord/rubber sheet is subjected to simple tension, an interesting deformation behavior occurs, which is not observed in most of the rigid composites. This can be elucidated by using Eq. (2.17) for the relation between γ_{xy} and the applied σ_{xx} as well as the approximations of Eqs. (8.4)

$$\gamma_{xy} = \bar{S}_{16}\sigma_{xx} \approx \frac{-2\sin\theta\cos^3\theta}{E_{22}}(2-\tan^2\theta)\sigma_{xx} \tag{8.6}$$

Thus, the stretching-shear coupling vanishes at $\theta \approx 54.7°$, and $\gamma_{xy} < 0$ for $\theta < 54.7°$ and $\gamma_{xy} = 0$ for $\theta > 54.7°$.

8.2.3 *Laminated composites*

The constitutive equations for the laminated cord/rubber composites are of the same general form as Eqs. (2.25)–(2.30). However, they can be simplified by using the approximated expressions of Eqs. (8.5) for $\bar{Q}_{ij}$. Also, the engineering elastic constants, referring to the x–y coordinate system, for the angle-ply laminated composite can be deduced. Using the results of Eqs. (8.4), the following expressions of engineering elastic constants of a $\pm\theta$ laminate in terms of the properties of fiber and matrix as well as the fiber volume fraction are obtained under the assumptions of $E_f \gg E_m$ and $\nu_m = 0.5$ (See Akasaka 1989, and Clark 1963a&b):

$$\begin{aligned}
E_{xx} &= E_f V_f \cos^4\theta + \frac{4G_m}{1-V_f} \\
&\quad - \frac{[E_f V_f \sin^2\theta\cos^2\theta + 2G_m/(1-V_f)]^2}{E_f V_f \sin^4\theta + 4G_m/(1-V_f)} \\
E_{yy} &= E_f V_f \sin^4\theta + \frac{G_m}{1-V_f} \\
&\quad - \frac{[E_f V_f \sin^2\theta\cos^2\theta + 2G_m/(1-V_f)]^2}{E_f V_f \cos^4\theta + 4G_m/(1-V_f)} \\
G_{xy} &= E_f V_f \sin^2\theta\cos^2\theta + \frac{G_m}{1-V_f} \\
\nu_{xy} &= \frac{E_f V_f \sin^2\theta\cos^2\theta + 2G_m/(1-V_f)}{E_f V_f \sin^4\theta + 4G_m/(1-V_f)} \\
\nu_{yx} &= \frac{E_f V_f \sin^2\theta\cos^2\theta + 2G_m/(1-V_f)}{E_f V_f \cos^4\theta + 4G_m/(1-V_f)}
\end{aligned} \tag{8.7}$$

The approach for obtaining Eqs. (8.7) based upon the assumptions of $\pm\theta$ cord angles and specially orthotropic symmetry is known as the *modified netting analysis*.

The classical netting analysis which assumes inextensible cords ($E_f \to \infty$) simplifies Eqs. (8.7)

$$\begin{aligned} E_{xx} &= 4G_m(1 - V_f)(\cot^4\theta - \cot^2\theta + 1) \\ E_{yy} &= E_{xx}(\pi/2 - \theta) \\ G_{xy} &= E_f V_f \sin^2\theta \cos^2\theta + G_m/(1 - V_f) \\ \nu_{xy} &= \cot^2\theta \\ \nu_{yx} &= \tan^2\theta \end{aligned} \tag{8.8}$$

Figures 8.3–8.5 show the results of analytical predictions based upon Eqs. (8.5) for E_{xx}, G_{xy}, and ν_{xy}, respectively, as functions of the off-axis angle θ. These results coincide very well with the experimental data, as reported by Clark (1963a&b) and based upon $E_{11} = 1440$ MPa and $E_{22} = 6.9$ MPa. It is evident that Poisson's ratios well in excess of one-half exist in cord/rubber composites.

Because of the incompressibility of the rubber matrix and the relatively small volume change associated with the cord materials, due to its high stiffness, it can be assumed that the cord/rubber composite is incompressible. Thus, for small strain, $\varepsilon_{xx} + \varepsilon_{yy} + \varepsilon_{zz} = 0$, and

$$\nu_{xz} = -\varepsilon_{zz}/\varepsilon_{xx} = 1 + \varepsilon_{yy}/\varepsilon_{xx} = 1 - \nu_{xy} \tag{8.9}$$

Figure 8.6 indicates the analytical results of Eq. (8.9) and the experimental data of ν_{xz} as a function of θ (Clark 1980) for

Fig. 8.3. Young's modulus, E_{xx}, vs. cord angle, θ, for a two-ply laminate. — Eqs. (8.7); (×) experimental data. (After Clark 1963a.)

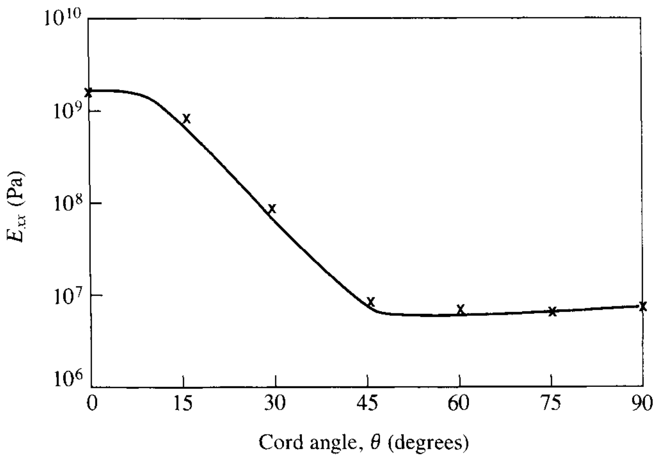

$E_{11} = 294$ MPa and $E_{22} = 6.6$ MPa. One of the solid lines is based upon the ν_{xy} expression of Eqs. (8.7), and the simplifying expression of Eqs. (8.4), namely

$$\nu_{xy} = \frac{E_{11}\sin^2\theta\cos^2\theta + E_{22}/2}{E_{11}\sin^4\theta + E_{22}} \tag{8.10}$$

The other solid line is based upon the ν_{xy} expression of Eqs. (8.8).

Fig. 8.4. Shear modulus, G_{xy}, vs. cord angle, θ, for a two-ply laminate. — Eqs. (8.7); (×) experimental data. (After Clark 1963a.)

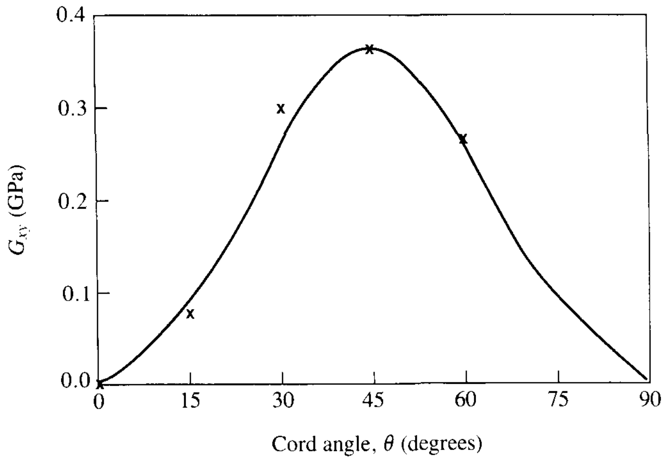

Fig. 8.5. Poisson's ratio, ν_{xy}, vs. cord angle, θ, for a two-ply laminate. — Eqs. (8.7); (×) experimental data. (After Clark 1963a.)

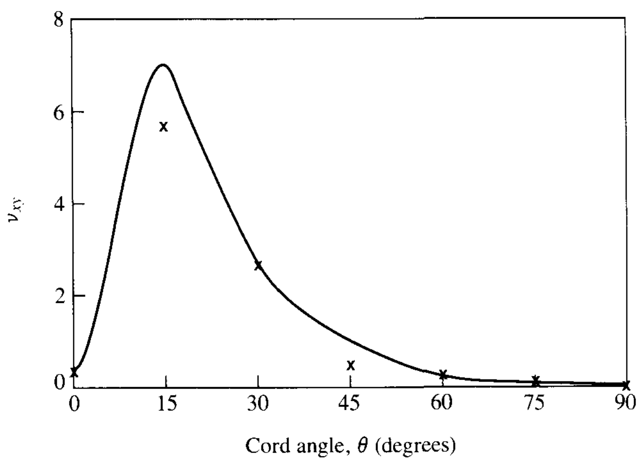

It is interesting to note that for a range of θ values, ν_{xz} is negative; the laminate becomes thicker under axial load.

The interlaminar stresses σ_{zz}, τ_{zx} and τ_{zy} are not considered in the classical lamination theory. These stresses and their corresponding strains do exist in appreciable magnitude which promote a reduction in the apparent stiffness of cord/rubber laminates. As a result, the composite becomes more flexible and exhibits lower natural frequencies of vibration and static buckling loads (Walter 1978).

Walter (1978) reviewed the work of Kelsey, who considered a two-ply $[\pm\theta]$ cord/rubber laminate, simulating the behavior of the belt in a radial tire. Assuming the belt of finite width in the y direction is loaded in the x (circumferential) direction, γ_{yz} vanishes due to symmetry and ε_{zz} is assumed to be negligibly small. γ_{xz} is maximum at the free edge of the belt and can be approximated, for the case of inextensible cords ($E_{\mathrm{f}} \to \infty$), by the simple expression

$$\gamma_{xz} = \varepsilon_{xx}(2\cot^2\theta - 1) \tag{8.11}$$

Equation (8.11) indicates that γ_{xz} vanishes when the two plies are oriented at $\theta = \pm\cot^{-1}\sqrt{(1/2)} = \pm 54.7°$. The magnitude of γ_{xz} decays exponentially away from the free edge and vanishes along the belt center-line ($y = 0$). It is interesting to note that $\theta = 54.7°$ is also the angle for which the normal stress and shear strain are uncoupled and each off-axis ply behaves as specially orthotropic.

Fig. 8.6. Poisson's ratio, ν_{xz}, vs. cord angle, θ, for a two-ply laminate. — Eqs. (8.8) and (8.10); (×) experimental data. (After Akasaka 1989.)

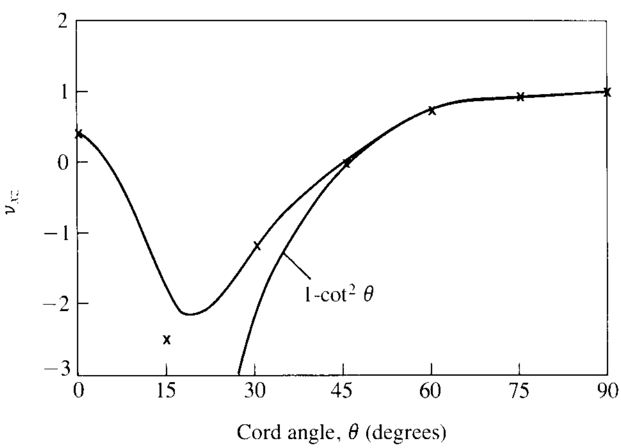

Interlaminar shear strains have been observed by inserting straight pins normal to the ply surface in a cord/rubber belt system and observing its rotation under extensional load (Bohm 1966) or by scribing a straight line on the edge of the specimen and monitoring the rotation of the line under load. Figure 8.7 shows the interlaminar shear strain measured by X-ray technique for a two-ply polyester–rubber as a function of cord angle θ (Lou and Walter 1978). The solid line is based upon the predictions of Eq. (8.11). The importance of interlaminar shear decreases as the number of plies increases.

Walter (1978) has presented values of the 18 elastic constants of A_{ij}, B_{ij} and D_{ij} for bias, belted-bias and radial constructions; the material combinations of nylon and rayon body plies with steel, PVA and rayon belt plies are included. For the case of a specially orthotropic laminate ($A_{16} = A_{26} = D_{16} = D_{26} = B_{ij} = 0$) with respect to the x–y axes, the out-of-plane flexural rigidities are

$$\begin{aligned}(EI)_x &= A_{11}h^2/12 = E_{11}h^3/12(1 - \nu_{xy}\nu_{yx})\\ (EI)_y &= A_{22}h^2/12 = E_{22}h^3/12(1 - \nu_{yx}\nu_{xy})\end{aligned} \tag{8.12}$$

where I is the area moment of inertia, and h denotes ply thickness.

8.2.4 *Cord loads in tires*

According to Clark (1980) the key to good tire design is long fatigue life. The loads on typical textile cords in pneumatic

Fig. 8.7. Interlaminar shear strain, γ_{xz}, vs. cord angle, θ, for a two-ply polyester rubber. — Eq. (8.11); (×) experimental data. (After Lou and Walter 1978.)

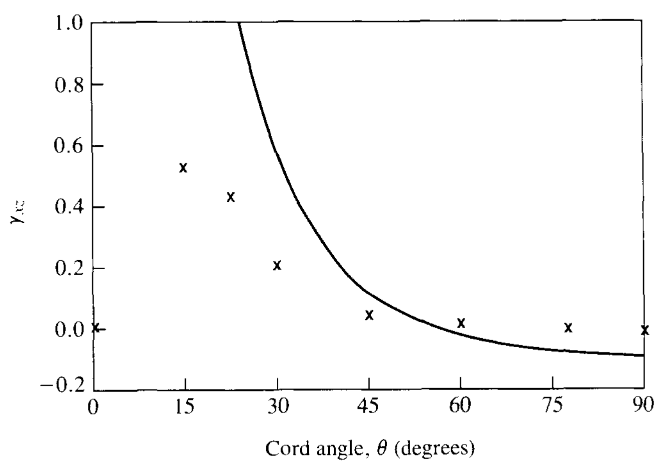

tires are extremely complex and the sources of loads can be identified as follows: (a) inflation load, (b) vertical load, (c) steering forces, (d) road irregularities, (e) camber, (f) speed, and (g) torque.

The tensile cord load due to inflation pressure can be predicted with some certainty by considering the axisymmetric nature of inflation and approximating the tire geometry as a thin toroidal shell. However, this task is complicated by the fact that the tire does not maintain a constant geometry during inflation. Furthermore, the membrane forces obtained from the thin shell analysis may not adequately represent the force distributions in the bead and tread regions. Figure 8.8 shows schematically the cross-section of a pneumatic tire and the designation of the locations (Clark 1980).

The measurement of cord loads is important to the analysis and design of tires. Various techniques have been employed; these include the use of grid or elongation marks for outer plies, X-ray photography relying on metal markers for inner plies, and resistance foil strain gages imbedded in the tire for direct cord load measurement in a tire under operating conditions. The force transducers using resistance foil strain gages are much smaller than the clip gages, the rubber–wire gages, or the liquid–metal gages. Details of these measurement techniques can be found in Clark and Dodge (1969), Patterson (1969), and Walter and Hall (1969).

The measurements of tire cord loads have indicated that the loads

Fig. 8.8. Location description in a cord/rubber pneumatic tire. (After Clark 1980.)

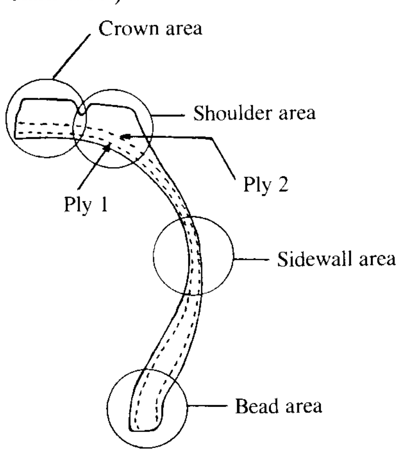

induced by normal direct inflation account for about 10–15% of cord strength. Another simple type of cord load is induced due to the load carried by the tire. The cord load at a given location can fluctuate fairly widely as the tire rolls. Also, the typical cord load cycle varies with the locations on the tire, i.e. crown, sidewall or shoulder region. Steering induces additional loads. Relatively small amounts of steer could induce very large increases in the cord loads. Figure 8.9 shows the basic characteristics of cord load fluctuation in a rolling tire (Clark 1980). It should be noted that compressive cord loads are possible. The characteristics of other cord loads due to road irregularities, speed and torque are even more difficult to quantify in a systematic manner.

The measurement of tire cord loads provides the basis of analysis of the response of cord/rubber composites to the specified boundary conditions. The netting theory, which only takes into account the deformation of the cord and neglects completely the contribution of the matrix rubber, was adopted in the earlier research on bias constructions. The uncertainty of the orientation of the cord in the net structure at different stress levels of inflation has limited the applicability of this theory.

The theory of laminated composites has undoubtedly provided an efficient means of analysis of cord/rubber composites. It is understood that the theory has its limitations due to the following reasons:

(1) Textile cord strains of several per cent could develop at some locations in the tire; even larger and nonlinear strains could develop in the rubber.

Fig. 8.9. Basic characteristics of cord load fluctuation in a rolling tire. (After Clark 1980.)

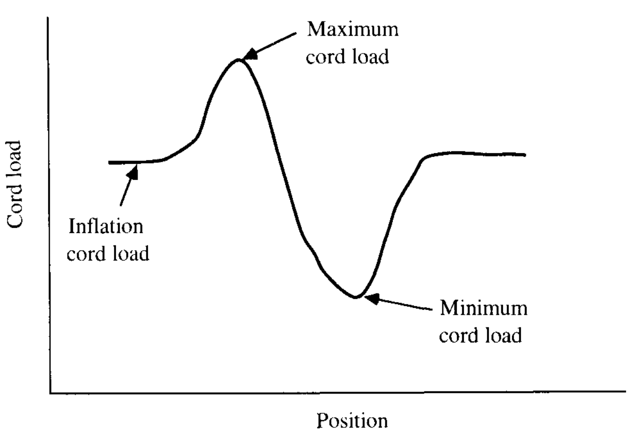

(2) Interlaminar deformations are not taken into account in the theory, assuming plane stress condition.
(3) Cord/rubber composites usually exhibit bimodulus behavior (Bert and Kumar 1981; Bert and Reddy 1982).
(4) The viscoelastic behavior is assumed to be small and is often neglected in the analysis.
(5) Perfect cord/rubber interfacial bonds are assumed.
(6) The membrane forces in the bead and tread regions may be very complex.
(7) Fatigue and hygrothermal loadings may also complicate the problem.

However, in spite of its limitations, the lamination theory has been applied with some success for investigating a number of tire mechanics problems including stress analysis, obstacle enveloping, treadwear, and vibration. It is thus an efficient tool based upon linearly elastic, homogeneous and anisotropic material properties for the representation of nonlinear viscoelastic, heterogeneous calendered plies of cord/rubber tire composites (Walter 1978). The large nonlinear deformation of flexible composites is treated in Chapter 9.

8.3 Coated fabrics

Coated fabrics used in load bearing environments, for instance, those for air- or cable-supported building structures, tents, and inflated structures such as escape slides, must exhibit specific mechanical properties. Some of the general requirements include retaining flexibility over a wide temperature range, sufficient tensile and tear strength, low air permeability, and sufficient dimensional stability (Skelton 1971).

It has been recognized that coated fabrics generally exhibit nonlinear stress–strain behavior due to straightening of the crimped yarns under uniaxial or biaxial tension. As noted by Akasaka (1989), the microscopic deformation behavior of the woven yarns embedded in the matrix and subjected to membrane loading is very complex. Thus, modeling of the strength behavior of these materials requires reasonably precise knowledge of the deformation of the yarns as a function of load configuration and magnitude.

The linear elastic properties of laminates composed of coated fabrics can be readily derived based upon the lamination theory of Section 2.3. Akasaka and Yoshida (1972) presented explicit expressions for elastic moduli of laminates of coated fabrics; the analytical predictions were compared with experimental data of laminates of canvas.

Skelton (1971), among others, reported the biaxial stress–strain behavior of coated orthogonal fabrics. It is concluded that the stress–strain response at various stages of manufacture of coated fabrics is dependent mainly on the crimp in the two sets of yarns.

Fig. 8.10. (a) A section of the fabric along warp yarns in off-loom (top), heat set (middle) and coated (bottom) states. (b) A section of the fabric along filling yarns in off-loom (top), heat set (middle) and coated (bottom) states. (c) Surface feature of the fabric in heat set state. (After Skelton 1971 © ASTM. Reprinted with permission.)

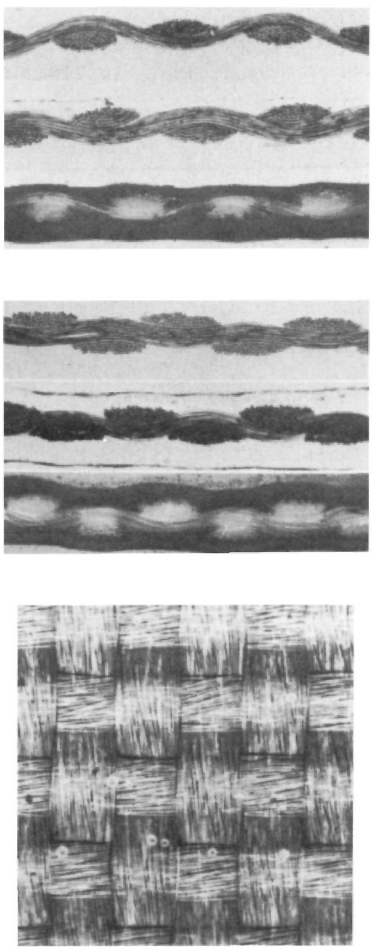

(a)

(b)

(c)

The balance of crimp is determined by the restraints imposed on the fabric during the heat setting process, which precedes the coating operation. If the fabric is set under tension in the warp direction, the warp yarns tend to become straight and the yarns in the filling direction become highly crimped. Thus, when such a fabric is subjected to biaxial loading, it is almost inextensible in the warp direction. Consequently, Skelton concluded that if a balanced fabric is required with similar biaxial tensile behavior in the warp and filling directions, the fabric must be heat set with both warp and filling directions under restraint.

It is interesting to recapitulate the experimental observations of Skelton (1971) for the biaxial testing of coated fabrics. Figures 8.10(a) and (b) show, respectively, the section views of a plain weave fabric based upon high tenacity polyester. Since the fabric is set under tension along the warp direction during heat setting, the warp crimp is minimum and the filling crimp is relatively high. Three stages, i.e. off-loom, heat set and coated state, are demonstrated. Figure 8.10(c) shows the surface features of the fabric in the heat set state.

Figure 8.11 shows the biaxial load–elongation curves for this

Fig. 8.11. Bi-axial load–elongation curves for a fabric; load ratio (warp/fill) = 1:2. WL = warp direction, loom state; FL = filling direction, loom state; WH = warp direction, heat set; FH = filling direction, heat set; WC = warp direction, coated; FC = filling direction, coated. (After Skelton 1971 © ASTM. Reprinted with permission.)

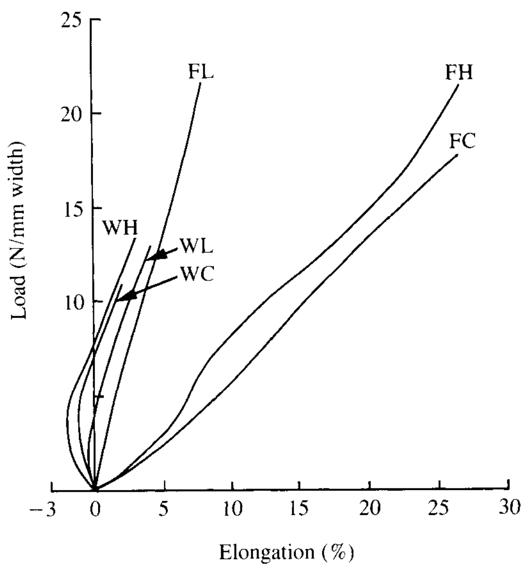

fabric with load ratio (warp/filling) = 1:2. The biaxial behavior can be understood by bearing in mind that in the heat set state the crimp is unbalanced; the warp yarns are essentially straight and the filling yarns are highly crimped. Thus, according to Skelton, the extension of the highly crimped direction of the filling yarns brings about an increase in crimp and reduction in width in the warp direction, in spite of the applied load in that direction. Consequently, the load–elongation curve shows negative elongation in the warp direction at low load level.

The elastic and inelastic responses of coated fabrics have been studied by Stubbs and Thomas (1984) and Stubbs (1988) using a space truss model. The model is capable of accounting for arbitrary loading sequences.

8.4 Nonlinear elastic behavior – incremental analysis

The flexible composites discussed in this section are also composed of continuous fibers in an elastomeric matrix. Because of the low shear modulus of the matrix and the highly anisotropic nature ($E_{11} \gg E_{22}$) of the composites, their effective elastic properties are very sensitive to the fiber orientation. The geometric nonlinearity of the flexible composite is mainly caused by the reorientation of fibers. The material nonlinearity is also pronounced in elastomeric composites under large deformation.

In order to fully realize the ability of the elastomeric matrix composite to sustain large deformation, Takahashi and Chou (1986), Takahashi, Kuo and Chou (1986), Chou and Takahashi (1987), and Takahashi, Yano, Kuo and Chou (1987) have predicted the nonlinear constitutive relation of flexible composites with sinusoidally shaped fibers based upon a step-wise incremental analysis and the classical lamination theory. In this section, the work of Chou and Takahashi is recapitulated. Both fiber geometric nonlinearity and matrix material nonlinearity have been taken into account. Because of the superposition of the infinitesimal solutions from lamination theory, the limitation of this approach is obvious. However, being a well established analytical technique in the composites field, the lamination theory does provide a convenient tool for discerning the basic characteristics of flexible composites.

Comparisons are made between the analytical predictions and experimental data for tire cord/rubber, and glass and Kevlar/silicone-elastomer flexible composite laminae. Since composites with fibers in wavy form have been used as a model system, the geometric aspects of curved fibers are examined first.

8.4.1 *Geometry of wavy fibers*

To demonstrate the effect of fiber extensibility from geometric design, a flexible composite composed of continuous fibers with sinusoidal waviness in a ductile matrix is used as a model system. Perfect bonding between the fibers and matrix is assumed. The geometric relations among the wavelength (λ), amplitude (a), and fiber length (s) of a sinusoidally shaped fiber are identified first. Then, two types of fiber arrangements are considered: the iso-phase model, and the random-phase model. The fibers are assumed to maintain the sinusoidal shape of which the geometric parameters λ, a and s vary with the increase of applied load.

The spatial position of a typical fiber in the xyz coordinates is given by:

$$y = a \sin \frac{2\pi x}{\lambda} \tag{8.13}$$

where the parameters a and λ of the curved fiber are shown in Fig.

Fig. 8.12. Geometrical relationships between a/λ, s/λ and θ_{max}, where θ_{max} is the maximum angle between the fiber and x axis. (After Chou and Takahashi 1987.)

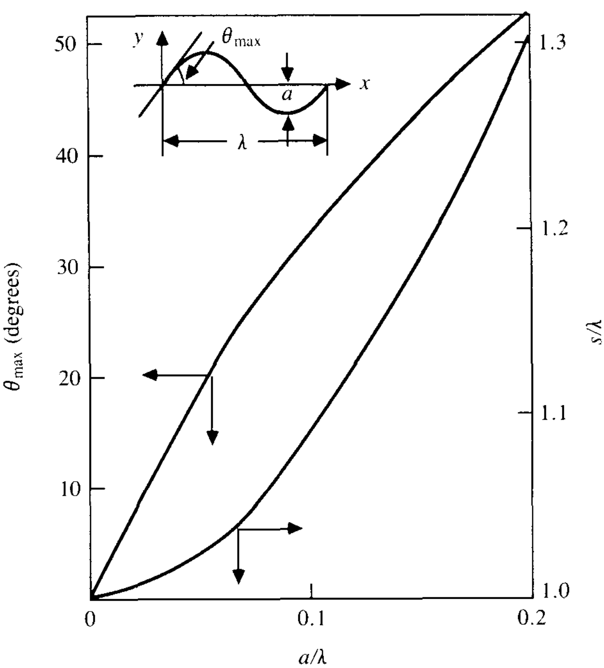

8.12. The angle θ between the tangent to the fiber and x axis is a function of x:

$$\tan\theta = \frac{\mathrm{d}y}{\mathrm{d}x} = \frac{2\pi a}{\lambda}\cos\frac{2\pi x}{\lambda} \tag{8.14}$$

The length of fiber, ds, between x and $x + \mathrm{d}x$ is

$$\mathrm{d}s = \sqrt{(\mathrm{d}x^2 + \mathrm{d}y^2)} = \mathrm{d}x\sqrt{\left[1 + c \cdot \cos^2\left(\frac{2\pi x}{\lambda}\right)\right]} \tag{8.15}$$

where

$$c = (2\pi a/\lambda)^2$$

Obviously, the maximum value of $\tan\theta$ occurs at

$$|\theta_{\max}| = \tan^{-1}\left(\frac{2\pi a}{\lambda}\right) \tag{8.16}$$

The fiber length, s, between $x = 0$ and λ is given by

$$s = \int \mathrm{d}s = \frac{\lambda}{2\pi}\int_0^{2\pi} \sqrt{(1 + c \cdot \cos^2\beta)}\,\mathrm{d}\beta \tag{8.17}$$

By the use of an elliptic integral of the second kind,

$$s = \lambda\sqrt{(1+c)}\left(1 - \frac{1}{2^2}k^2 - \frac{1^2 \cdot 3}{2^2 \cdot 4^2}k^4 - \frac{1^2 \cdot 3^2 \cdot 5}{2^4 \cdot 4^2 \cdot 6^2}k^6 - \cdots\right) \tag{8.18}$$

where

$$k^2 = \frac{c}{1+c} \tag{8.19}$$

Equation (8.18) can be rewritten as

$$\frac{s}{\lambda} = \frac{1}{\sqrt{(1-k^2)}}\left(1 - 2\left(\frac{k^2}{8}\right) - 3\left(\frac{k^2}{8}\right)^2 - 10\left(\frac{k^2}{8}\right)^3 - \frac{175}{4}\left(\frac{k^2}{8}\right)^4 - \frac{441}{2}\left(\frac{k^2}{8}\right)^5 - \cdots\right) \tag{8.20}$$

By the use of Taylor expansion, we have

$$\frac{s}{\lambda} = 1 + 2\left(\frac{k^2}{8}\right) + 13\left(\frac{k^2}{8}\right)^2 + 90\left(\frac{k^2}{8}\right)^3 + 644\left(\frac{k^2}{8}\right)^4 + 4708.5\left(\frac{k^2}{8}\right)^5 + \cdots \tag{8.21}$$

In the following analysis, terms up to $(k^2/8)^5$ in Eq. (8.21) are taken into account, and the range of a/λ is limited to below $\frac{1}{5}$. The relationship between a/λ and s/λ is shown in Fig. 8.12 where θ_{max} is the maximum angle between the fiber and the x axis. For example, for $\theta_{max} = 20°$, $a/\lambda = 0.058$ and $s/\lambda = 1.032$. The curved fiber composite with $a/\lambda = 0.10$ can be extended up to 9.23% of its original length only by the straightening of the fiber, if the matrix stiffness is negligible.

Two kinds of arrangements of the curved fibers in the composite have been considered: the iso-phase model and random-phase model. The iso-phase model is defined in Fig. 8.13, where all the fibers are in the same phase in the x direction. The distance between the fibers in the y direction is assumed to be constant. In the random phase model (Fig. 8.14), the axial locations of sinusoidal shaped fibers do not assume any regular pattern.

8.4.2 *Axial tensile behavior*

The nonlinear tensile stress–strain behavior of flexible composites containing wavy fibers has been investigated according to the iso-phase and random-phase models. The lamination theory described in Section 2.3 is the basis of this analysis. The applied load is parallel to the axes of the sinusoidally shaped fibers.

8.4.2.1 *Iso-phase model*

The linear elastic stress–strain relations are derived first. Consider Fig. 8.13; each volume element between x and $x + dx$ is

Fig. 8.13. Iso-phase model. (After Chou and Takahashi 1987.)

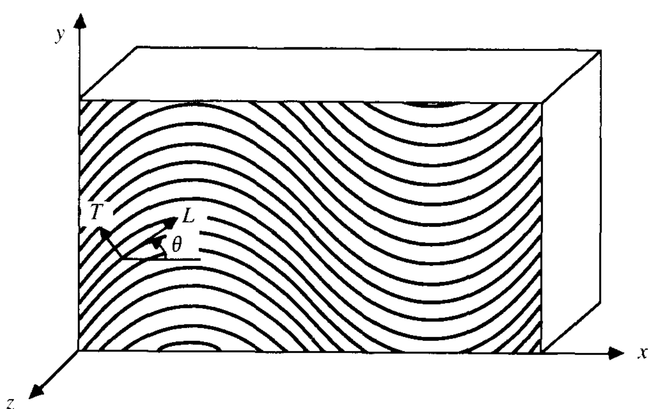

approximated by a unidirectional straight fiber composite, in which fibers are inclined at an angle θ to the x axis, as defined by Eq. (8.14). The transformation of coordinates between the composite reference axes (xyz) and the fiber local axes (LTz) is given by:

$$\begin{pmatrix} L \\ T \\ z \end{pmatrix} = \begin{pmatrix} \cos\theta & \sin\theta & 0 \\ -\sin\theta & \cos\theta & 0 \\ 0 & 0 & 1 \end{pmatrix} \begin{pmatrix} x \\ y \\ z \end{pmatrix} \tag{8.22}$$

The positive direction of θ is defined in Fig. 8.13. Under the uniaxial tension, σ_{xx}, Eq. (2.17) gives

$$\begin{aligned} \varepsilon_{xx} &= \bar{S}_{11}\sigma_{xx} \\ \varepsilon_{yy} &= \bar{S}_{12}\sigma_{xx} \\ \gamma_{xy} &= \bar{S}_{16}\sigma_{xx} \end{aligned} \tag{8.23}$$

It is interesting to note the stretching–shear coupling represented by $\bar{S}_{16}$. Figure 8.15 shows schematically the γ_{xy} induced by an applied stress σ_{xx}.

The average tensile strain of the iso-phase composite, ε^*_{xx}, is

$$\varepsilon^*_{xx} = \frac{1}{\lambda}\int_0^\lambda \varepsilon_{xx}\,\mathrm{d}x \tag{8.24}$$

Fig. 8.14. Random-phase model. (After Chou and Takahashi 1987.)

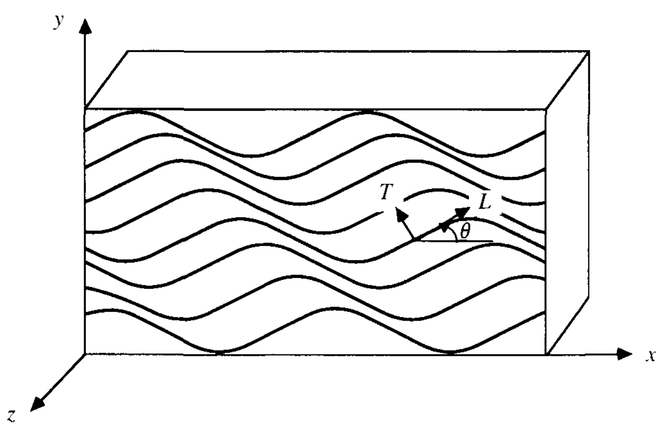

From Eqs. (8.14) and (8.23),

$$\varepsilon_{xx}^{*} = \left[\frac{1+\frac{c}{2}}{(1+c)^{3/2}} S_{11} - \left(\frac{1+\frac{3}{2}c}{(1+c)^{3/2}} - 1 \right) S_{22} + \frac{\frac{c}{2}}{(1+c)^{3/2}} (2S_{12} + S_{66}) \right] \sigma_{xx} \tag{8.25}$$

The effective Young's modulus of the iso-phase model in the x direction is given by

$$E_{xx}^{*} = \frac{(1+c)^{3/2}}{\left(1+\frac{c}{2}\right)S_{11} - \left(1+\frac{3}{2}c - (1+c)^{3/2}\right)S_{22} + \frac{c}{2}(2S_{12}+S_{66})} \tag{8.26}$$

In a small volume element between x and $x + dx$, the tensile strain of the fiber along its axial direction is expressed by

$$\varepsilon_{\mathrm{L}} = \varepsilon_{xx} \cos^2 \theta + \varepsilon_{yy} \sin^2 \theta + \gamma_{xy} \sin \theta \cos \theta \tag{8.27}$$

Substituting Eqs. (8.23) into Eq. (8.27) and integrating over s, the average fiber axial strain is

$$\varepsilon_{\mathrm{L}}^{*} = \frac{1}{s} \int_0^s \varepsilon_{\mathrm{L}} \, ds = [(S_{11} - S_{12})F(k) + S_{12}]\sigma_{xx} \tag{8.28}$$

where

$$F(k) = 1 - \frac{1}{2}k^2 - \frac{3}{16}k^4 - \frac{3}{32}k^6 - \frac{111}{2048}k^8 - \frac{141}{4096}k^{10} \tag{8.29}$$

Fig. 8.15. Schematic illustration of the deformed shape of the iso-phase model under uniaxial tension σ_{xx}. (After Chou and Takahashi 1987.)

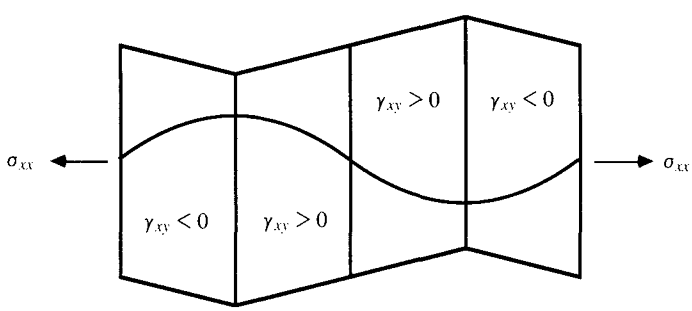

Here, the relations among s, x and λ, Eqs. (8.14)–(8.20), and the elliptic integral are used in the derivations.

8.4.2.2 *Random-phase model*

In the case of the iso-phase model, the stretching–shear coupling constants $\bar{S}_{16}$ and $\bar{S}_{26}$ do not vanish. This coupling effect could be eliminated through the random positioning of wavy fibers along the x-direction:

$$y = a \sin(2\pi(x-d)/\lambda) \tag{8.30}$$

where d is the translation of the fiber in the x direction. A random distribution of d ($0 \le d \le \lambda$) is assumed in this model. That is, in each infinitesimal section, dx, fibers with any arbitrary orientation angles exist with the same probability. Therefore, it is assumed that ε_{xx} is uniform throughout the sample under uniaxial tension. The stress in a fiber segment depends on its orientation, θ:

$$-\frac{2\pi a}{\lambda} \le \tan\theta \le \frac{2\pi a}{\lambda}$$

By these assumptions, the classical lamination theory can again be applied.

The stress–strain relations of a unidirectional lamina consisting of straight fibers are given by Eq. (2.13) with the reduced stiffness Q_{ij} given by Eqs. (2.14). The transformed stress–strain relations of an off-axis lamina, referring to the x–y coordinate system, are given by Eqs. (2.15) and (2.16). The small element of the random-phase composite situated between the sections at x and $x + \mathrm{d}x$ is treated as a laminate with different orientations. The fibers with the orientation angle θ which lies in the range defined by

$$0 \le \theta \le \tan^{-1}\left(\frac{2\pi a}{\lambda}\right) \tag{8.31}$$

have the probability $\mathrm{d}x/\lambda$.

Therefore, the stress–strain relation of the laminate can be rewritten as

$$\begin{pmatrix} \sigma_x \\ \sigma_y \\ \tau_{xy} \end{pmatrix} = \begin{pmatrix} C_{11}^* & C_{12}^* & C_{16}^* \\ C_{12}^* & C_{22}^* & C_{26}^* \\ C_{16}^* & C_{26}^* & C_{66}^* \end{pmatrix} \begin{pmatrix} \varepsilon_x \\ \varepsilon_y \\ \gamma_{xy} \end{pmatrix} \tag{8.32}$$

where

$$C_{mn}^* = \frac{1}{\lambda}\int_0^{\lambda} Q_{mn}(\theta)\,\mathrm{d}x \tag{8.33}$$

The average stiffness constants of Eq. (8.33) are

$$\begin{aligned}
C_{11}^* &= \frac{1}{(1+c)^{3/2}}\left[Q_{11}\left(1+\frac{c}{2}\right)+(Q_{12}+2Q_{66})c\right.\\
&\quad\left.+Q_{22}\left((1+c)^{3/2}-\left(1+\frac{3}{2}c\right)\right)\right]\\
C_{22}^* &= \frac{1}{(1+c)^{3/2}}\left[Q_{11}\left((1+c)^{3/2}-\left(1+\frac{3}{2}c\right)\right)\right.\\
&\quad\left.+(Q_{12}+2Q_{66})c+Q_{22}\left(1+\frac{c}{2}\right)\right]\\
C_{12}^* &= \frac{1}{(1+c)^{3/2}}\left[(Q_{11}+Q_{22}-4Q_{66})\frac{c}{2}+Q_{12}((1+c)^{3/2}-c)\right]\\
C_{66}^* &= \frac{1}{(1+c)^{3/2}}\left[(Q_{11}+Q_{22}-2Q_{12}-2Q_{66})\frac{c}{2}\right.\\
&\quad\left.+Q_{66}((1+c)^{3/2}-c)\right]\\
C_{16}^* &= C_{26}^* = 0
\end{aligned} \tag{8.34}$$

Inversion of Eq. (8.32) leads to

$$\begin{pmatrix}\varepsilon_{xx}\\ \varepsilon_{yy}\\ \gamma_{xy}\end{pmatrix}=\begin{pmatrix}S_{11}^* & S_{12}^* & 0\\ S_{12}^* & S_{22}^* & 0\\ 0 & 0 & S_{66}^*\end{pmatrix}\begin{pmatrix}\sigma_{xx}\\ \sigma_{yy}\\ \tau_{xy}\end{pmatrix} \tag{8.35}$$

where

$$\begin{aligned}
S_{11}^* &= (C_{22}^*C_{66}^* - C_{26}^{*2})/D\\
S_{22}^* &= (C_{11}^*C_{66}^* - C_{16}^{*2})/D\\
S_{12}^* &= (C_{16}^*C_{26}^* - C_{12}^*C_{16}^*)/D\\
S_{66}^* &= (C_{11}^*C_{22}^* - C_{12}^{*2})/D\\
D &= C_{11}^*C_{22}^*C_{66}^* - C_{12}^{*2}C_{66}^*
\end{aligned} \tag{8.36}$$

Following Eqs. (2.9), the Young's modulus and Poisson's ratio in the x direction of the random-phase model are given by:

$$\begin{aligned}
E_{xx}^* &= 1/S_{11}^*\\
\nu_{xy}^* &= -S_{12}^*/S_{11}^*
\end{aligned} \tag{8.37}$$

If the random-phase model is subjected to uniaxial tension, σ_{xx}, the strain components are

$$\begin{aligned} \varepsilon_{xx} &= \sigma_{xx}/E^*_{xx} \\ \varepsilon_{yy} &= -(\nu^*_{xy}/E^*_{xx})\sigma_{xx} \\ \gamma_{xy} &= 0 \end{aligned} \tag{8.38}$$

The strain of the fiber in its axial direction is calculated by substituting Eqs. (8.38) into Eq. (8.27) and averaging over s (Eq. (8.28))

$$\varepsilon^*_{\mathrm{L}} = (\varepsilon_{xx} - \varepsilon_{yy})F(k) + \varepsilon_{yy} \tag{8.39}$$

where $F(k)$ is given by Eq. (8.29).

8.4.2.3 *Nonlinear tensile stress–strain behavior*

The nonlinear axial (x direction) tensile stress–strain behavior of the flexible composite is examined using the stepwise incremental analysis of Petit and Waddoups (1969). Consider an incremental tensile strain Δe_{xx}, applied on either the iso-phase or random-phase model. Here, $\Delta e_{xx} = \Delta l/l$; Δl and l are the incremental length and the current length, respectively. Using the initial Young's modulus E^*_{xx}, the first stress increment, $\Delta\sigma_{xx}$, is calculated by the linear elastic relation:

$$\Delta\sigma_{xx} = E^*_{xx}\,\Delta e_{xx} \tag{8.40}$$

where the expressions of E^*_{xx} are given by Eqs. (8.26) and (8.37) for the iso-phase and random-phase models, respectively. The nth stress increment is added to the previous stress state after $n-1$ increments to determine the current total stress:

$$(\sigma_{xx})_n = (\sigma_{xx})_{n-1} + (\Delta\sigma_{xx})_n \tag{8.41}$$

For the iso-phase model, the average tensile strain increment of the fiber along its axial direction, Δe^*_{L}, is obtained by substituting Eq. (8.40) into Eq. (8.28):

$$\Delta e^*_{\mathrm{L}} = [(S_{11} - S_{12})F(k) + S_{12}]\,\Delta\sigma_{xx} \tag{8.42}$$

For the random-phase model, the transverse strain increment, Δe_{yy}, is determined from Δe_{xx} and ν^*_{xy}:

$$\Delta e_{yy} = -\nu^*_{xy}\,\Delta e_{xx} \tag{8.43}$$

Then, the tensile strain increment of the fiber is calculated by substituting Δe_{xx} and Δe_{yy} into Eq. (8.39):

$$\Delta e^*_{L} = (\Delta e_{xx} - \Delta e_{yy})F(k) + \Delta e_{yy} \tag{8.44}$$

The total strain, referring to the current specimen length, after n increments is

$$e_{xx} = \sum_{i=1}^{n} (\Delta e_{xx})_i = \sum_{i=1}^{n} \left(\frac{\Delta l}{l}\right)_i \tag{8.45}$$

Replacing Δl by the infinitesimal increment, dl, it follows:

$$e_{xx} = \int_{l_o}^{l} \frac{dl}{l} = \ln\frac{l}{l_o} = \ln(1 + \varepsilon_{xx}) \tag{8.46}$$

Here, ε_{xx} is the tensile strain referred to the initial specimen length l_o:

$$\varepsilon_{xx} = \frac{l - l_o}{l_o} \tag{8.47}$$

In the range of large strain, the use of ε_{xx} is more convenient than the summation of Δe_{xx}. From Eq. (8.46)

$$\varepsilon_{xx} = \exp(e_{xx}) - 1 \tag{8.48}$$

Then, the total strain, after the nth increment, in the axial direction (ε_{xx}), transverse direction (ε_{yy}) and the fiber (ε_L^*) are given by:

$$(\varepsilon_{xx})_n = \exp\left[\sum_{i=1}^{n} (\Delta e_{xx})_i\right] - 1 \tag{8.49}$$

$$(\varepsilon_{yy})_n = \exp\left[\sum_{i=1}^{n} (\Delta e_{yy})_i\right] - 1 \tag{8.50}$$

$$(\varepsilon_L^*)_n = \exp\left[\sum_{i=1}^{n} (\Delta e_L^*)_i\right] - 1 \tag{8.51}$$

Finally, the change of fiber shape under loading needs to be taken into account. Due to the tensile loading in the x direction, the wavelength of the curved fiber is changed to

$$\lambda = \lambda_o(1 + \varepsilon_{xx}) \tag{8.52}$$

where λ and λ_o are, respectively, the current and initial values of the wavelength, and the total strain ε_{xx} is given by Eq. (8.49). The current value of the fiber length is

$$s = s_o(1 + \varepsilon_L^*) \tag{8.53}$$

where s_o is the initial fiber length and ε_L^* is the total fiber strain given by Eq. (8.51).

In order to determine the shape of the fiber, it is assumed that the fiber maintains a sinusoidal waviness during deformation while varying its amplitude (a) and wavelength (λ). The current value of the amplitude, a, can be determined by Fig. 8.12 from the given current values of λ and s. The values of $k^2 = c/(1+c)$, $c = (2\pi a/\lambda)^2$, E^*_{xx} and ν^*_{xy} after the nth step are determined from the current values of λ and a, and these values are used in the $(n+1)$th step of the incremental analysis. Eqs. (8.41) and (8.49) give the uniaxial tensile stress–strain relation of the flexible composite.

The elastic constants of fibers (Chamis 1984) and matrices (*Modern Plastics Encyclopedia* 1983) used in the numerical calculations of Chou and Takahashi (1987) are shown in Table 8.1. Linear elastic stress–strain relations are assumed for glass and Kevlar fibers. Rubber elasticity (James and Guth 1943; Treloar 1973) is assumed for PBT and the other elastomeric polymers:

$$\sigma = \frac{E^{\mathrm{o}}_{\mathrm{m}}}{3}\left(\alpha - \frac{1}{\alpha^2}\right) \tag{8.54}$$

where $E^{\mathrm{o}}_{\mathrm{m}}$ is the initial Young's modulus of the matrix, and α is the extension ratio:

$$\alpha = 1 + \varepsilon_{xx} \tag{8.55}$$

The secant Young's modulus of the matrix, E_{m}, is determined from the current tensile strain, ε_{xx}, (Eqs. (8.49) and (8.55)):

$$E_{\mathrm{m}} = \frac{\mathrm{d}\sigma}{\mathrm{d}\varepsilon_{xx}} = \frac{E^{\mathrm{o}}_{\mathrm{m}}}{3}\left(1 + \frac{2}{\alpha^3}\right) \tag{8.56}$$

Numerical examples of the stress–strain relations predicted by the incremental analysis are shown in Figs. 8.16 and 8.17. The results indicate that Kevlar is less effective than glass fiber in contributing

Table 8.1. *Elastic constants and elongations* (*Chou and Takahashi* 1987)

	E_{L} (GPa)	E_{T} (GPa)	G_{LT} (GPa)	ν_{LT}	ν_{TT}	ε_{b} (%)
Glass fiber	72.52		29.7	0.22		4
Kevlar	151.6	4.13	2.89	0.35	0.35	3.5
PBT matrix	2.156		0.77	0.4		50–300

Isotropic relation $G = E/2(1+\nu)$ is assumed.

Fig. 8.16. Comparisons of the effects of glass and Kevlar fibers on the tensile stress (σ_{xx})–strain (ε_{xx}) curves for an iso-phase composite at various E_m^o. Rubber elasticity is assumed for the matrix. Crosses (×) show average fiber axial tensile strain; ε_L^* reaches 4% and 3.5% for glass and Kevlar fibers, respectively. $\nu_m = 0.4$, $V_f = 50\%$, $a/\lambda = 0.1$. (After Chou and Takahashi 1987.)

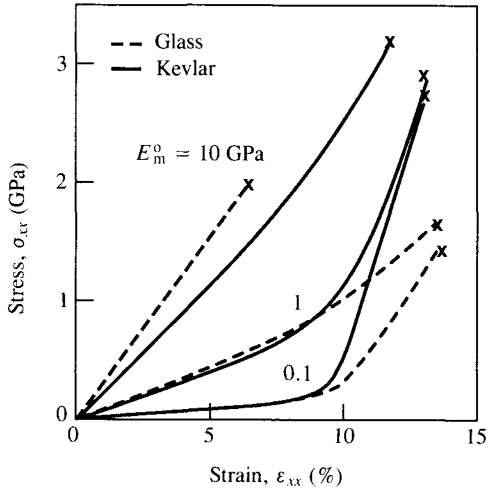

Fig. 8.17. Tensile stress (σ_{xx})–strain (ε_{xx}) curves of Kevlar/PBT polymer composites predicted by using the iso-phase (solid line) and random-phase (dotted line) models. $E_m^o = 1$ GPa, $\nu_m = 0.4$ and $V_f = 50\%$. Crosses (×) show average fiber axial tensile strain; ε_L^* reaches 3.5%. (After Chou and Takahashi 1987.)

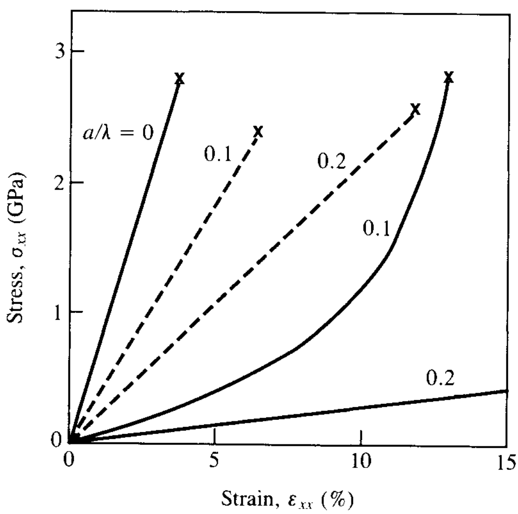

to the stiffness of curved fiber composites, because the transverse Young's modulus of Kevlar is lower than that of glass. After the wavy fibers are stretched, however, Kevlar becomes increasingly more effective with regard to stiffness and strength (Fig. 8.16). For a given wavy fiber composite, the random-phase model predicts higher Young's modulus and lower elongation than those of the iso-phase model (Fig. 8.17).

8.4.3 *Transverse tensile behavior*

The transverse tensile behavior of wavy fiber composites has been analyzed for both iso-phase and random-phase models by Kuo, Takahashi and Chou (1988). The lamination theory is again the basis of the incremental analysis.

8.4.3.1 *Iso-phase model*

Consider the small volume element situated between y and $y + \mathrm{d}y$ in the iso-phase model as shown in Fig. 8.13. It is assumed that the transverse stress σ_{yy} is uniformly distributed along one wavelength λ. Then an element of the size $\mathrm{d}y\,\mathrm{d}x$ can be treated as an off-axis unidirectional lamina. From Eq. (2.17) and plane stress condition, the strain components in this element are

$$\varepsilon_{xx} = \bar{S}_{12}\sigma_{yy} \qquad \varepsilon_{yy} = \bar{S}_{22}\sigma_{yy} \qquad \gamma_{xy} = \bar{S}_{26}\sigma_{yy} \tag{8.57}$$

Then the transverse strain averaged over the wavelength of the iso-phase model is

$$\varepsilon_{yy}^{*} = \frac{1}{\lambda}\int_0^{\lambda} \varepsilon_{yy}\,\mathrm{d}x \tag{8.58}$$

The effective Young's modulus in the y direction is

$$\begin{aligned} E_{yy}^{*} &= \frac{\sigma_{yy}}{\varepsilon_{yy}^{*}} \\ &= \frac{(1+c)^{3/2}}{\left((1+c)^{3/2} - 1 - \dfrac{3c}{2}\right)S_{11} + \left(1 + \dfrac{c}{2}\right)S_{22} + \dfrac{c}{2}(2S_{12} + S_{66})} \end{aligned} \tag{8.59}$$

Following the approach of Section 8.4.2.1, the average tensile strain along the fibers due to transverse tension is obtained by substituting Eqs. (8.57) into Eq. (8.27) and averaging over the length s:

$$\varepsilon_{\mathrm{L}}^{*} = [(S_{12} - S_{11})F(k) + S_{11}]\sigma_{yy} \tag{8.60}$$

$F(k)$ is given by Eq. (8.29).

Kuo, Takahashi and Chou (1988) also analyzed the transverse tensile behavior based upon the constant strain assumption. This assumption is validated by the observation during transverse tension experiments that the elongation of the specimen is uniform throughout its width away from the specimen ends. Although the constitutive relations are not of the same form for constant stress and constant strain analyses, the numerical calculations in Kuo, Takahashi and Chou (1988) yield the same result. This is the direct consequence of the approaches, namely the stress (or strain) is considered in the average sense along the x direction.

8.4.3.2 *Random-phase model*

The transverse Young's modulus and minor Poisson's ratios are given by

$$\begin{aligned} E^*_{yy} &= 1/S^*_{22} \\ v^*_{yx} &= -S^*_{12}/S^*_{22} \end{aligned} \tag{8.61}$$

Fig. 8.18. Comparisons between theoretical predictions and experimental data of transverse tension of an iso-phase model. Specimen initial $a/\lambda = 0.05$–0.07 and $V_f = 1.337\%$ for Thornel-300/silicone elastomer composites. (After Kuo, Takahashi and Chou 1988.)

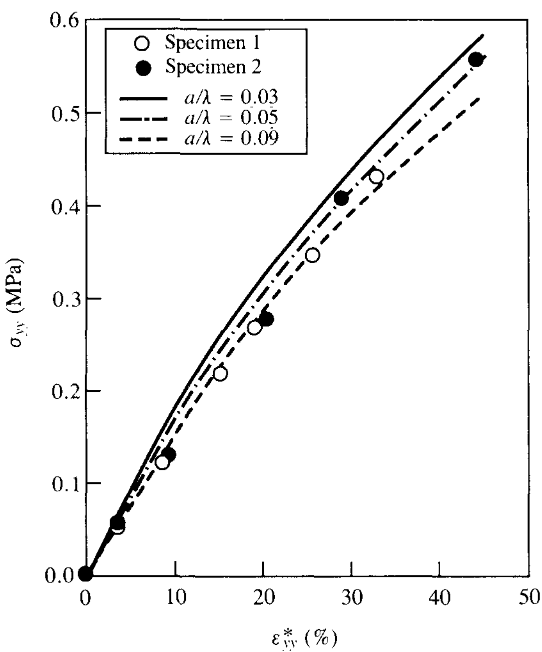

Under the transverse stress, σ_{yy}, the strain components are

$$\begin{aligned} \varepsilon_{xx} &= -(\nu^*_{yx}/E^*_{yy})\sigma_{yy} \\ \varepsilon_{yy} &= \sigma_{yy}/E^*_{yy} \\ \gamma_{xy} &= 0 \end{aligned} \tag{8.62}$$

Again, the average tensile strain along the fiber is obtained from Eq. (8.39).

Figure 8.18 depicts the comparison between theoretical curves and experimental data of an iso-phase model under transverse tension. The experimental material system reported by Kuo, Takahashi and Chou (1988) is based upon Sylgard 184 silicone elastomer reinforced with Thornel-300 carbon fiber. A loose fiber bundle contains 1000 filaments, with a filament diameter of 7 μm. The specimen fabrication technique follows that given by Luo and Chou (1988). The initial a/λ values of the specimens are in the range of 0.05–0.07. The fiber volume fraction is very low, about 1.34%.